Stability of Jahn-Teller distortion ordering in LaMn$_{1-x}$Sc$_x$O$_3$

V. Cuartero,[1,*] J. Blasco,[2] G. Subías,[2] J. García,[2] C. Meneghini,[3] and G. Aquilanti[4]

[1]*ESRF-The European Synchrotron, 71, Avenue des Martyrs, Grenoble, France*

[2]*Instituto de Ciencia de Materiales de Aragón, Departamento de Física de la Materia Condensada, CSIC-Universidad de Zaragoza, C/ Pedro Cerbuna 12, 50009 Zaragoza, Spain*

[3]*Dipartimento di Scienze, Università di Roma TRE, Via della Vasca Navale 84 – 00146, Roma, Italy*

[4]*Elettra-Sincrotrone Trieste, s.s. 14, km 163.5, 34149 Basovizza, Trieste, Italy*

We have investigated the role of Mn^{3+} Jahn-Teller distortion in driving ferromagnetism in the LaMn$_{1-x}$Sc$_x$O$_3$ series. The replacement of Mn by Sc in LaMnO$_3$ decreases the orthorhombic distortion of the *Pbnm* cell, but the unit cell remains distorted even in the LaScO$_3$ sample. The analysis of the x-ray diffraction patterns indicates a continuous evolution from the typical Jahn-Teller distorted octahedron in LaMnO$_3$ into a nearly regular one in LaScO$_3$. Surprisingly, x-ray absorption spectroscopy measurements at the Mn and Sc *K* edges reveal the stability of both Jahn-Teller distorted MnO$_6$ octahedron and nearly regular ScO$_6$ octahedron along the whole Sc-substituted series. Moreover, the structure is described as a random distribution of Jahn-Teller distorted MnO$_6$ octahedra spatially ordered as in LaMnO$_3$ and nearly regular ScO$_6$ octahedra. This result contrasts with the pseudocubic phase and the appearance of regular MnO$_6$ octahedra in LaMn$_{1-x}$Ga$_x$O$_3$ for $x > 0.5$. Thus the occurrence of Jahn-Teller distortion strongly depends on the distorted orthorhombic crystallographic structure of the matrix in which the Mn^{3+} atom is allocated. Besides, a ferromagnetic ground state is observed for $x > 0.5$ in both series independently of the presence (or not) of Jahn-Teller distortions around Mn^{3+}, which discards either the spin flipping or the vibronic superexchange models proposed for the ferromagnetism in LaMn$_{1-x}$B$_x$O$_3$ (B = Sc or Ga).

I. INTRODUCTION

The exotic properties of RMnO$_3$ (R = rare earth) perovskites are being extensively exploited for the manufacturing of thin films or artificial heterostructures for technological applications [1]. The quantum correlations between charge, spin, and structural degrees of freedom are playing the main role in the different phenomena observed on these materials. In particular, LaMnO$_3$ is considered the mother compound of the magnetoresistance manganites and the prototype of the co-operative Jahn-Teller systems and orbital-ordered state [2–4].

LaMnO$_3$ is a paramagnetic insulator at room temperature with an orthorhombic unit cell (space group *Pbnm*) [3,5,6]. Its structure can be viewed as a spatial ordering of tetragonal distorted MnO$_6$ octahedra, i.e., alternating short and long Mn-O bonds in the *ab* plane. The electronic configuration for a Mn^{3+} ion is $3d^4$ in the ionic approach. The octahedral crystalline field splits the *d* states into t_{2g} and e_g orbitals, and the electronic degenerate e_g state couples with the local phonon modes of the same symmetry [Jahn-Teller (JT) effect]. This gives rise to the tetragonal distortion of the octahedron and a simultaneous splitting of the e_g electronic states. LaMnO$_3$ develops long-range magnetic ordering below $T_N = 140$ K that is antiferromagnetic (AFM) of type A [3,6]. The Mn moments lie along the (010) direction with the spins coupled ferromagnetically in the *ab* plane and antiferromagnetically coupled along the *c* axis.

Both the crystal structure and the magnetic ordering are strongly affected by hole doping. It is well known that the replacement of La by a divalent cation [7,8] leads to

compounds showing colossal magnetoresistance, which are metallic ferromagnets at low temperature with reduced tetragonal deformation in the MnO$_6$ octahedron [9,10]. Moreover, oxygen excess also induces ferromagnetism in LaMnO$_{3-\delta}$ samples [6]. The origin of these changes is similar and it lies on the emergence of an intermediate valence state of the Mn ion originated by either the doping or the lack of oxygen stoichiometry. The double exchange interaction mechanism between Mn^{3+}/Mn^{4+} ions was proposed to explain ferromagnetism [11], and the electron-phonon coupling is thought to be conducted via the JT effect [12–14]. Besides that, the substitution of Mn by other transition metals also induces ferromagnetism (FM) for certain concentrations of the doping species [15–20]. In some cases, this behavior is also related to a change in the Mn valence state. We have verified that ferromagnetism in LaMn$_{1-x}$Ni$_x$O$_3$ can be explained by the strong superexchange FM interaction between Mn^{4+} and Ni^{2+} [21]. The substitution of Mn by nonmagnetic isovalent ions such as Ga^{3+} ($3d^{10}$) or Sc^{3+} ($3d^0$) has particular importance, since this perturbation at the Mn atom should not affect its electronic state and consequently, its local electronic and geometrical structure would not be modified. Therefore the magnetic and transport properties would only be affected by the effect of the dilution of Mn sublattice. Surprisingly, this substitution favors the appearance of a ferromagnetic ground state [18,21–23]. Several interpretations have been given to account for the appearance of the ferromagnetic ordering in this last case [15–17,24,25]. Goodenough *et al.* [17,19] proposed that ferromagnetism is originated by the ferromagnetic vibronic superexchange interaction coming from the disordered and fluctuating JT-distorted Mn^{3+} ions. On the other hand, Farrell and Ghering [24] suggested that the e_g orbital in JT-distorted Mn^{3+} surrounded by gallium or

---

*Corresponding author: cuartero@esrf.fr

scandium transforms from the $(3x^2 - r^2)/(3y^2 - r^2)$ states into the $3z^2 - r^2$ state (spin-flipping model). Both models assume that the change from A-type AFM to FM ordering is originated by the orbital direction adopted by the Mn^{3+} ion and it is similar for Ga and Sc nonmagnetic substitutions, so the atomic e_g orbital would be perturbed in the same way for the two series.

This explanation contrasts with the experimental determination of the local geometrical structure of the Mn atom by x-ray absorption spectroscopy (XAS) for $LaMn_{1-x}Ga_xO_3$. It has been shown that the tetragonal distortion of MnO_6 octahedron continuously decreases with the gallium content in such a way that for $x > 0.5$ MnO_6 distortion disappears and becomes regular, simultaneously to a long-range FM ground state [26,27]. Dynamical tetragonal distortions have been discarded as well, considering the shortest time of the x-ray absorption process [28]. On the other hand, despite the similarity of the magnetic behavior of Ga and Sc series, the crystallographic structure evolves in a clearly different way along the two dilutions. Whereas for the Ga-substituted samples the cell parameters $(a, b, c/2^{1/2})$ converge to the same value for $x = 0.5$ [17,22], pointing out a nearly cubic unit cell, the Sc-doped cell parameters do not converge for any concentration (x) [19]. Moreover, an XAS study of the isostructural $TbMn_{1-x}Sc_xO_3$ series showed that the MnO_6 octahedra remain tetragonally distorted along the whole dilution range, independently of the Sc content [29].

In order to clarify the role of the JT distortion in the emergence of ferromagnetism in isovalent Mn-site substituted $LaMnO_3$, we have studied the crystallographic structure by x-ray powder diffraction (XRD) and the local structure at the Mn and Sc sites by XAS of $LaMn_{1-x}Sc_xO_3$ compounds. The combination of the structural parameters obtained by XRD (coherent periodicity) and those obtained by XAS (incoherent average) allows us to microscopically describe the changes after Sc substitution. This study also reveals the similarities and differences with the Ga-substituted series and allows us to determine the role of the Mn-sublattice dilution over the local structural distortions in driving ferromagnetism after Ga/Sc substitution.

II. EXPERIMENTAL

Powder $LaMn_{1-x}Sc_xO_3$ ($x = 0, 0.1, 0.2, 0.3, 0.4, 0.5, 0.6,$ $0.7, 0.9, 1$) samples were synthesized following a conventional ceramic procedure. Stoichiometric amounts of La_2O_3, $MnCO_3$, and Sc_2O_3 were mixed, milled, and fired at $1250\,°C$ during 24 h in air. This step was repeated one more time after pressing the powder into pellets. Finally, the pellets were milled, repressed, and sintered at $1400\,°C$ for 48 h in an argon atmosphere. The samples were stoichiometric with the accuracy (± 0.02) given by the standard redox titration method.

XRD patterns were collected for the whole series in the $2 - \theta$ range between $18°$ and $135°$ at room temperature by using a D-max Rigaku system with a rotating anode and selecting the Cu $K\alpha$ radiation. The patterns were consistent with a perovskite single phase for the whole series. The crystal structures were refined by the Rietveld method using the FULLPROF program [30].

X-ray absorption measurements at the Mn and Sc K edges were carried out with a Si(111) double-crystal monochromator at the BM23 beamline of the ESRF (Grenoble, France) and the CLAESS beamline of the ALBA (Barcelona, Spain) synchrotron facilities. Mn K-edge data were recorded at a fixed temperature ($T \sim 80\,K$) in transmission mode for Sc concentrations up to $x = 0.7$, while for $x = 0.9$, fluorescence detection was used. The Sc K-edge XAS measurements were carried out in transmission mode at liquid nitrogen temperature at the CLAESS beamline of the ALBA synchrotron for Sc concentrations $x > 0.4$. Data for $x < 0.4$ were recorded at room temperature with fluorescence detection. In the $LaMn_{0.4}Sc_{0.6}O_3$ sample, temperature-dependent XAS spectra were collected at the Sc K edge between 80 and 300 K at the XAFS beamline of the Elettra synchrotron [31] and at the Mn K edge from 50 to 300 K at the BM23 beamline of the ESRF.

The x-ray absorption near edge structure (XANES) spectra were normalized to unity edge jump using the ATHENA software DEMETER package [32]. The extraction of the extended x-ray absorption fine-structure (EXAFS) $\chi(k)$ signals was also performed using the ATHENA program, and R-space EXAFS spectra were obtained by calculating the Fourier transform (FT) of the $k^2\chi(k)$ signals in different k ranges, depending on the edges (see more details below), using a sinus window. The EXAFS structural analysis was performed using theoretical phases and amplitudes calculated by the FEFF-6 code [33], and fits to the experimental data were carried out in R space with the ARTEMIS program of the DEMETER package [32].

III. RESULTS

A. X-ray powder diffraction

All the XRD patterns were refined using an orthorhombic cell belonging to the *Pbnm* space group (no. 62, standard *Pnma*). Table I shows relevant structural parameters of the refinements, and Fig. 1(a) shows the evolution of the room-temperature cell parameters with the Sc content. The lattice parameters refined for the $LaMnO_3$ sample are in agreement with the results obtained in Ref. [20], confirming the right oxygen stoichiometry. By increasing the Sc content, the orthorhombic distortion decreases and a smooth crossover from the axial ratio $c/\sqrt{2} < a$ to $c/\sqrt{2} > a$ occurs near $x = 0.3$, where the O' phase ($c/\sqrt{2} < a < b$) is lost. The unit-cell volume increases linearly ($22.5\,\text{Å}^3/x$) with increasing x (Sc content), as corresponds to the ionic radius of a sixfold-coordinated Sc^{3+}, $0.745\,\text{Å}$, larger than that of a sixfold-coordinated Mn^{3+} (high spin), $0.645\,\text{Å}$. These results agree with those already published by Goodenough *et al.* [19] regarding the variation of the cell parameters and volume dependence for the orthorhombic $LaMn_{1-x}Sc_xO_3$ series. However, the evolution of the cell parameters along this series is markedly different from that in the Ga-substituted samples [17,22] [Fig. 1(b)]. The orthorhombic distortion decreases as Mn is replaced by Sc, but the unit cell remains distorted even in the $LaScO_3$ sample, whereas this orthorhombic distortion almost disappears for $x > 0.5$ in the $LaMn_{1-x}Ga_xO_3$ system ($a \approx b \approx c/\sqrt{2}$). Moreover, a O' phase is retained up to $x = 0.5$ in the Ga-substituted samples.

TABLE I. Refined structural parameters (unit cell, fractional coordinates, bond lengths, and bond angles) and reliability factors from the x-ray diffraction patterns at room temperature in the $LaMn_{1-x}Sc_xO_3$ series.

	$x = 0.1$	$x = 0.2$	$x = 0.3$	$x = 0.4$	$x = 0.5$	$x = 0.6$	$x = 0.7$	$x = 0.9$	$x = 1$
a(Å)	5.5445(2)	5.5604(1)	5.5711(1)	5.5866(1)	5.6016(1)	5.6176(1)	5.6334(1)	5.6683(2)	5.6796(1)
b(Å)	5.6990(2)	5.7061(1)	5.704(1)	5.7120(1)	5.7217(1)	5.7343(1)	5.7488(1)	5.7699(2)	5.7912(1)
c(Å)	7.7712(3)	7.8337(2)	7.8779(2)	7.9168(2)	7.9514(2)	7.9849(1)	8.0145(2)	8.0719(3)	8.0951(1)
La: x	0.9927(4)	0.9919(3)	0.9913(2)	0.9902(3)	0.9898(2)	0.9893(2)	0.9889(3)	0.9901(3)	0.9892(2)
y	0.0442(3)	0.0432(2)	0.0427(1)	0.0416(1)	0.0411(1)	0.0415(1)	0.0411(2)	0.0432(1)	0.0432(1)
B(Å^2)	0.12(4)	0.08(2)	0.13(2)	0.23(2)	0.20(2)	0.16(2)	0.08(8)	0.12(2)	0.14(1)
Mn/Sc : B(Å^2)	0.32(6)	0.21(4)	0.06(3)	0.11(3)	0.09(3)	0.05(3)	0.17(4)	0.25(4)	0.39(3)
O1: x	0.0812(27)	0.0881(23)	0.0777(12)	0.0751(19)	0.0739(17)	0.0854(16)	0.0775(20)	0.0865(20)	0.0873(14)
y	0.4830(23)	0.4904(13)	0.4863(14)	0.4847(15)	0.4801(14)	0.4797(14)	0.4787(17)	0.4747(15)	0.4711(13)
B(Å^2)	0.84(19)	0.93(16)	0.77(13)	0.74(14)	0.80(13)	0.78(12)	0.67(15)	0.69(14)	0.42(9)
O2: x	0.7238(26)	0.7203(18)	0.7171(13)	0.7107(14)	0.7077(13)	0.7076(12)	0.7026(14)	0.7010(15)	0.7011(10)
y	0.3059(22)	0.3074(13)	0.3050(11)	0.3031(12)	0.3042(11)	0.3031(11)	0.3047(13)	0.2979(14)	0.2995(10)
z	0.0284(21)	0.0274(11)	0.0367(8)	0.0372(10)	0.0377(9)	0.0376(9)	0.0375(11)	0.0458(11)	0.0498(8)
B(Å^2)	0.84(19)	0.93(16)	0.77(13)	0.74(14)	0.80(13)	0.78(12)	0.67(15)	0.69(14)	0.42(9)
M-O1 (Å)	1.998(5)	2.019(3)	2.018(2)	2.025(2)	2.034(2)	2.056(2)	2.054(2)	2.082(3)	2.090(2)
M-O2 (Å)	2.151(9)	2.150(8)	2.138(7)	2.114(8)	2.115(7)	2.114(6)	2.112(7)	2.095(8)	2.115(6)
M-O2 (Å)	1.902(9)	1.916(9)	1.951(7)	1.990(8)	2.006(7)	2.016(6)	2.039(7)	2.090(8)	2.096(6)
$\langle M$-O1-$M \rangle$ (deg)	153.1(2)	151.8(1)	154.8(1)	155.6(1)	155.6(1)	152.2(1)	154.6(1)	151.4(1)	151.0(1)
$\langle M$-O2-$M \rangle$ (deg)	157.6(4)	156.8(4)	154.3(3)	153.4(3)	152.5(3)	152.7(3)	151.6(3)	150.2(3)	148.7(2)
R_{Bragg}(%)	5.8	5.2	3.4	5.6	4.6	4.3	5.1	2.5	4.6
R_{wp}/R_F(%)	11.7/2.8	8.4/2.9	7.0/2.5	8.4/2.7	7.6/2.5	7.3/2.5	9.2/2.8	8.2/1.7	7.8/2.5

Regarding the MO_6 octahedron (M = Mn/Sc), we observe that the nearly tetragonal distorted MnO_6 in $LaMnO_3$ continuously evolves to a nearly regular one in $LaScO_3$, as appreciated in Fig. 2(a), where the interatomic distances between M and oxygen atoms are plotted. Alternatively, the MO_6 distortion disappears for $x = 0.5$ in the $LaMn_{1-x}Ga_xO_3$ series, being the octahedron regular for $x > 0.5$ [see Fig. 2(b)]. A similar decrease in the MO_6 distortion is observed in $LaMn_{1-x}Al_xO_3$ ($x \leqslant 0.2$) [19]. The comparison of these results shows that the effect of the isovalent substitution of nonmagnetic atoms

depends strongly on the trivalent doping metal. Moreover, the overall M-O-M angles decrease (octahedral tilts increase) by $8°$ when Mn is completely substituted with Sc, which is just opposite to what it is found on the $LaMn_{1-x}Ga_xO_3$ series [22].

B. X-ray absorption spectroscopy, XANES

The normalized Mn K-edge XANES spectra of selected $LaMn_{1-x}Sc_xO_3$ samples ($x = 0.0, 0.3, 0.5, 0.6,$ and 0.9) at room temperature are shown in Fig. 3. The spectra are

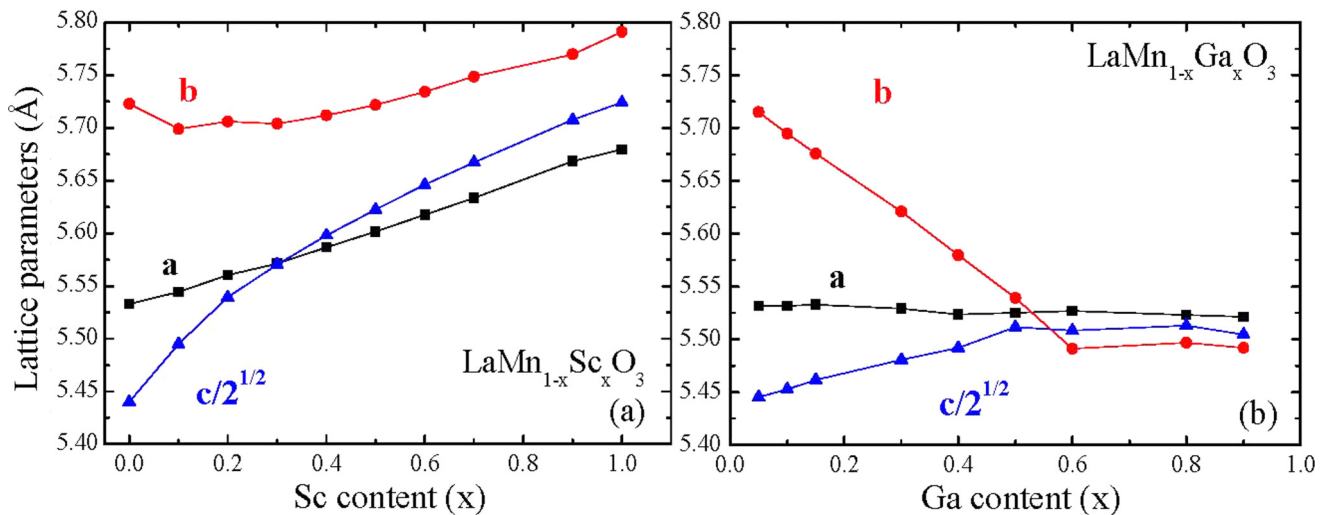FIG. 1. (Color online) Room-temperature unit-cell parameters of the $LaMn_{1-x}Sc_xO_3$ (panel a) and $LaMn_{1-x}Ga_xO_3$, taken from [22] (panel b) systems.
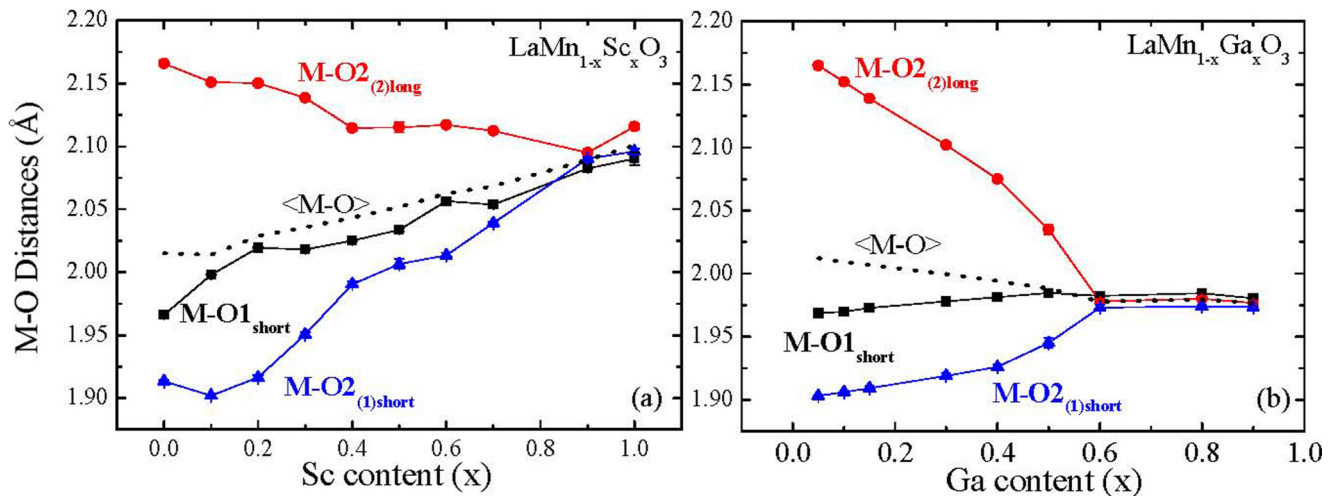
FIG. 2. (Color online) Bond lengths of the M-O sublattice in $LaMn_{1-x}Sc_xO_3$ (panel a) and $LaMn_{1-x}Ga_xO_3$ (panel b) [22].

characterized by a main resonance at the absorption edge corresponding to $1s - \varepsilon p$ transitions and a prepeak structure below the main absorption edge. This prepeak structure is displayed in more detail in the inset. All the spectra are nearly identical, showing that the local structure around the Mn atom remains nearly unaltered, except for subtle changes in the intensity of the main resonance. We also observe that there is no edge energy shift with Sc substitution (the maximum chemical shift is lower than 0.1 eV). This shows that the formal Mn valence is 3+ for the whole series [34]. Two structures can be individuated on the preedge region at 6540 and 6542.4 eV, which are attenuated by raising the Sc content, showing almost the same intensity independently of the Sc content. These features are normally ascribed to either dipole-forbidden or quadrupolar transitions from $1s \rightarrow 3d$ states, being the $3d$ states hybridized with $2p$ oxygen states in the latter case [35]. It seems that Sc $3d$ states show weaker hybridization with the oxygen p and consequently, the intensity of the prepeaks decrease after Sc substitution.
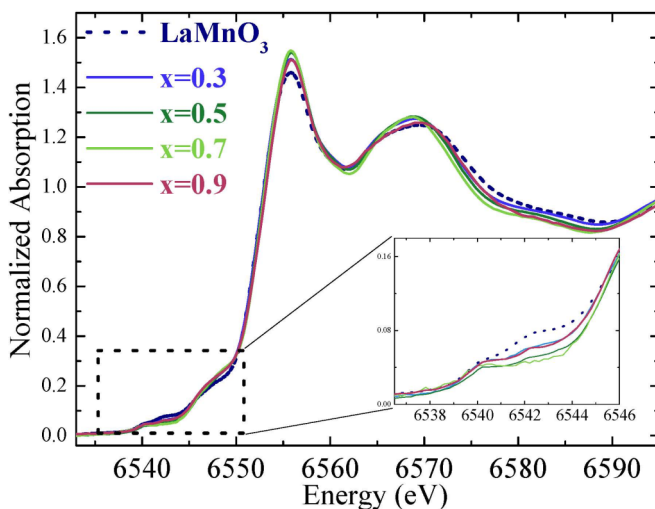
Figure 4 shows the normalized XANES spectra for selected $LaMn_{1-x}Sc_xO_3$ ($x = 0.3$, 0.4, 0.6, 0.7, and 1) samples at the Sc K edge. The spectra are very similar to each other, indicating that the local electronic and geometrical structures around Sc do not change along the series either. Besides, the chemical shift is unappreciable, which confirms the stability of the 3+ formal valence of Sc. Finally, the prepeak intensity of the feature at 4493 eV appears only for the Mn-substituted samples, being absent in $LaScO_3$ and very low for $LaMn_{0.1}Sc_{0.9}O_3$, as shown in the inset of Fig. 4. This result is in agreement with the model previously described for the features on the preedge region.

C. Extended x-ray absorption fine structure, EXAFS

EXAFS measurements at the Mn K edge were carried out in two experimental stations: BM23 at the ESRF and CLAESS at ALBA synchrotron facilities, resulting in equal spectra that guarantees the reliability of the data. Figure 5(a)
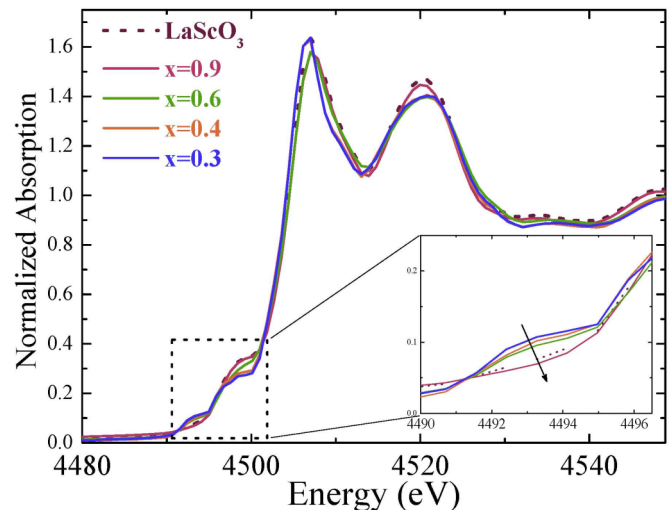

FIG. 3. (Color online) Normalized Mn K-edge XANES spectra of the $LaMn_{1-x}Sc_xO_3$ samples. Inset: zoom from the preedge region.

FIG. 4. (Color online) Comparison of the normalized XANES spectra of the $LaMn_{1-x}Sc_xO_3$ samples at the Sc K edge. Inset: zoom of the preedge region. The arrow indicates increase of Sc content.

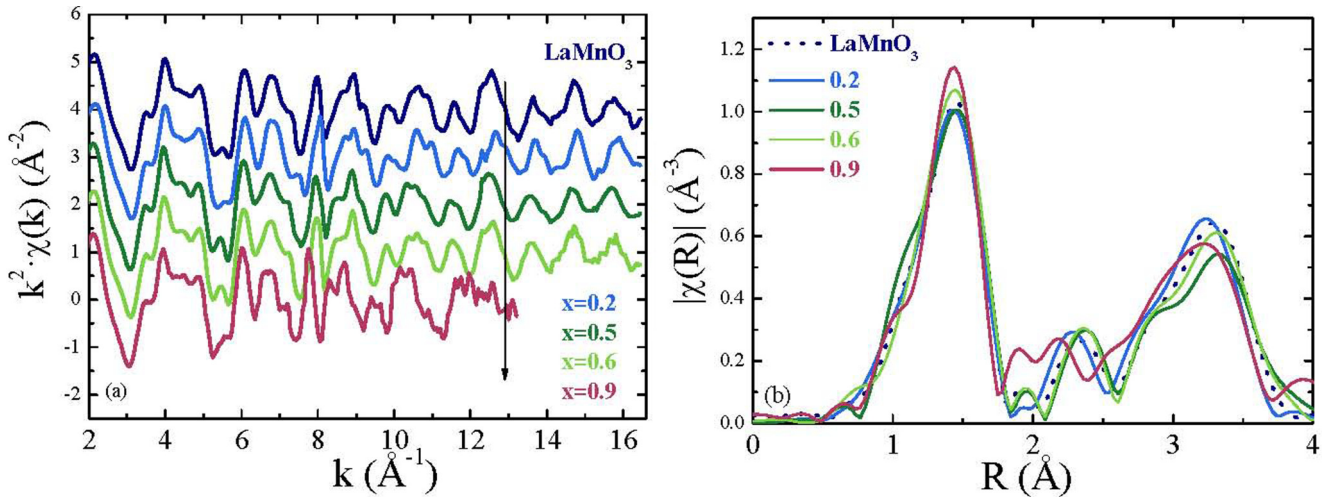FIG. 5. (Color online) (a) $k^2\chi(k)$ EXAFS signals and (b) modulus of the FT at the Mn K edge for selected $LaMn_{1-x}Sc_xO_3$ samples. $T = 80$ K.

displays Mn K-edge $k^2\chi(k)$ EXAFS signals and Fig. 5(b) the modulus of the FT. The most diluted Mn sample ($x = 0.9$) was measured in fluorescence mode using a Vortex silicon drift detector, and in this case the FT was obtained using a sine window between 2.5 and 13 Å^{-1}, due to the limitations on the signal-to-noise ratio at higher k values [see Fig. 5(a)]. For matters of comparison, the FTs shown on Fig. 5(b) are obtained using the same k range (2.5–13 Å^{-1}) and a sinus window. The first main peak at $\sim$1.5 Å corresponds to the first oxygen coordination shell. The intensity and shape of this peak are practically independent of the dilution, indicating that the oxygen coordination geometry around the Mn atom remains almost unaltered along the series up to the highly diluted Sc samples. Further peaks appear between 2 and 3.5 Å, which correspond to single scattering contributions of the Mn-Mn(Sc) and Mn-La next-nearest-neighbors paths and the Mn-O-Mn multiple scattering path. Only subtle

changes in the shape and intensity of these peaks are evidenced in the FT spectra in Fig. 5(b).

The starting model used to fit the data was the crystallographic structure of $LaMnO_3$. Coordination numbers were fixed to their crystallographic values, and the amplitude reduction factor S_0^2 was fixed to 0.8 for all samples, as it is the value obtained on the fit of the parent compound. Only bond lengths, Debye-Waller factors (σ^2), and the energy shift parameter (E_0) were refined. The local structural analysis was made up to 4.2 Å in two different k ranges, from 2.5 to either 16 or 13 Å^{-1}. The latter short k range was used to properly compare all measurements, including the spectra measured in fluorescence for the highly diluted sample with $x = 0.9$, that shows a low signal-to-noise ratio at high k values. The fits of the distances were performed considering the same shift on the equatorial plane (Mn-O1$_{short}$ and Mn-O2$_{short}$, delr$_1$) and a different one for the apical distance (Mn-O2$_{long}$, delr$_2$) of the MnO_6 octahedron. Similar structural parameters were obtained within the experimental error for the two sets of fits. Fits for selected compounds are shown in Fig. 6 and Table II summarizes the relevant structural parameters for
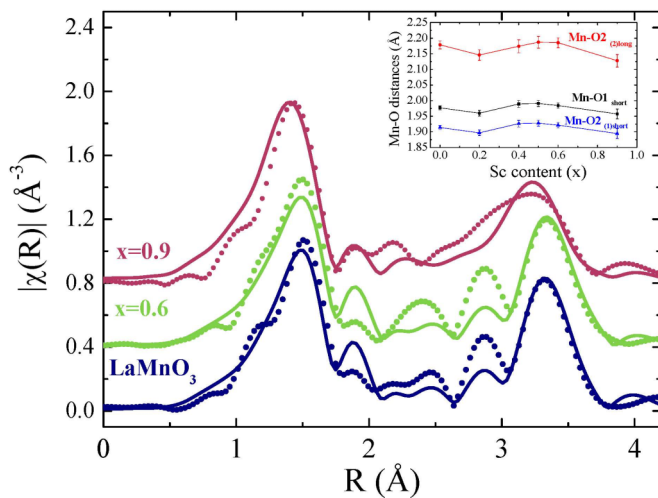

FIG. 6. (Color online) Fits (lines) of the FT signal from k^2-weighted EXAFS signals ($T = 80$ K) of selected samples until $R = 4.2$ Å. Inset: Mn-O distances, according to the results described in Table I.

TABLE II. Interatomic Mn-O distances and Debye-Waller factors for the first Mn-O shell in $LaMn_{1-x}Sc_xO_3$. S_0^2 was fixed to 0.8 as a result of the fit from the parent compound. The k range corresponds to $k_{min} = 2.5$ Å^{-1}, $k_{max} = 16$ Å^{-1} ($k_{max} = 13$ Å^{-1} for the $x = 0.9$ sample). The fit was performed in R space weighted in k^2, being $R_{min} = 1$ Å, $R_{max} = 4.2$ Å, and $dR = 0.2$. The E_0 parameter ranged between -0.3 and -2 eV. The results correspond to spectra measured at $T = 80$ K.

	Mn-O2$_{short}$	Mn-O1	Mn-O2$_{long}$	$\sigma^2 \times 10^{-3}$(Å^2)	R_{factor}
$LaMnO_3$	1.91(1)	1.98(1)	2.18(1)	1.6(1)	0.02
$x = 0.2$	1.90(1)	1.96(1)	2.15(2)	2.5(7)	0.04
$x = 0.4$	1.93(1)	1.99(1)	2.17(2)	2.4(9)	0.05
$x = 0.5$	1.93(1)	1.99(1)	2.19(2)	2.5(9)	0.05
$x = 0.6$	1.92(1)	1.98(1)	2.18(2)	2.1(7)	0.04
$x = 0.9$	1.90(1)	1.96(1)	2.13(2)	1.4(1)	0.04

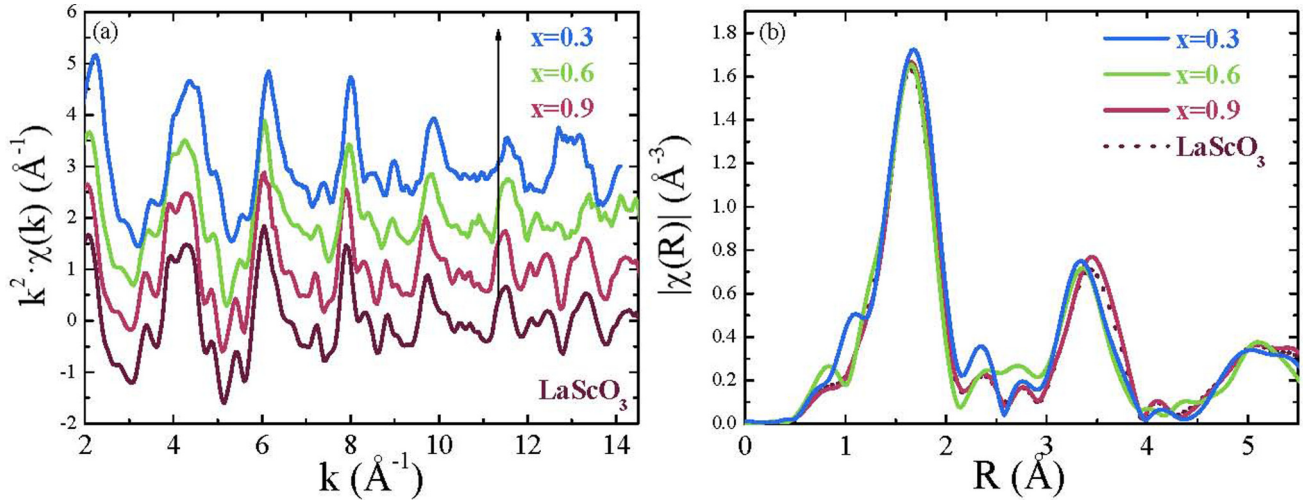FIG. 7. (Color online) (a) $k^2\chi(k)$ EXAFS signals and (b) modulus of the FT at the Sc K edge for selected LaMn$_{1-x}$Sc$_x$O$_3$ samples. All the spectra are measured at $T = 80$ K, except for $x = 0.3$, measured in fluorescence at room temperature.

the first oxygen coordination shells of all samples. The same tetragonal distorted (JT) MnO$_6$ as in LaMnO$_3$ is found for all Sc substitutions. It corresponds to two short pairs and one long pair of Mn-O interatomic distances, and the magnitude of this tetragonal distortion does not change with increasing dilution of Mn^{3+}. Similar behavior was already observed in TbMn$_{1-x}$Sc$_x$O$_3$ series [29], whereas in the LaMn$_{1-x}$Ga$_x$O$_3$, this MnO$_6$ distortion continuously diminishes and disappears for $x > 0.5$ [26,27].

EXAFS spectra were also measured at the Sc K edge in order to complete the local structural study. Figure 7(a) displays Sc K-edge $k^2\chi(k)$ EXAFS signals, and Fig. 7(b) shows the modulus of the FT using a sine window between 2.5 and 14 Å^{-1} for the LaMn$_{1-x}$Sc$_x$O$_3$ ($x = 0.3, 0.4, 0.6, 0.9$, and 1) samples. The EXAFS spectra along the series are nearly identical to that of LaScO$_3$, and the local structure around the Sc atom seems to be nearly unaltered across the whole series,

which is evidenced in the comparison of the modulus of the FTs, similar to the results reported at the Mn K edge.

The structural analysis was performed including coordination shells up to 5 Å using the crystallographic structure of LaScO$_3$. This corresponds to three pairs of Sc-O interatomic distances slightly distorted (2.09, 2.1, and 2.11 Å). We have performed the fitting considering these three independent Sc-O paths, but all the fits converge to a unique Sc-O interatomic distance. Fits for selected compounds are shown in Fig. 8, and Table III summarizes the relevant structural parameters for the first oxygen coordination shell of all samples. S_0^2 was fixed to 0.9, which is the value found for the LaScO$_3$ sample. As shown in the inset of Fig. 8, the fit of the EXAFS spectra shows the same distribution of Sc-O distances as in the LaScO$_3$ sample for all Sc concentrations. Therefore the ScO$_6$ octahedron remains almost regular along the whole dilution.

We have also tested the crystallographic distortion of the LaMn$_{0.4}$Sc$_{0.6}$O$_3$ sample by fitting the data with the three pairs of Sc-O distances distorted by 2.013, 2.06, and 2.12 Å (XRD data for this composition). As pointed out above, the best fit resulting from the slightly distorted octahedral model for the Sc-substituted samples is similar to the former model,

FIG. 8. (Color online) Fits (lines) of the FT signal from k^2-weighted EXAFS signals of selected samples until $R = 5$ Å. Inset: Sc-O distance, according to the results described in Table III.

TABLE III. Interatomic Sc-O distances and Debye-Waller factors for the first Sc-O shell in LaMn$_{1-x}$Sc$_x$O$_3$. S_0^2 was fixed to 0.9 as a result of the fit from the parent compound. The k range corresponds to $k_{min} = 2.5$ Å^{-1}, $k_{max} = 14$ Å^{-1}. The fit was performed in R space weighted in k^2, being $R_{min} = 1$ Å, $R_{max} = 5.5$ Å and $dR = 0.2$. The E_0 parameter ranged between -0.3 and -2 eV. All spectra are measured in transmission at $T = 80$ K, except for $x = 0.3, 0.4$ which are measured in fluorescence at room temperature.
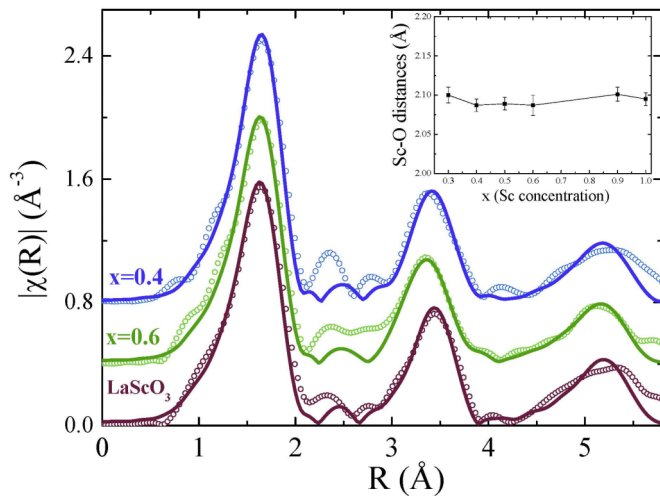
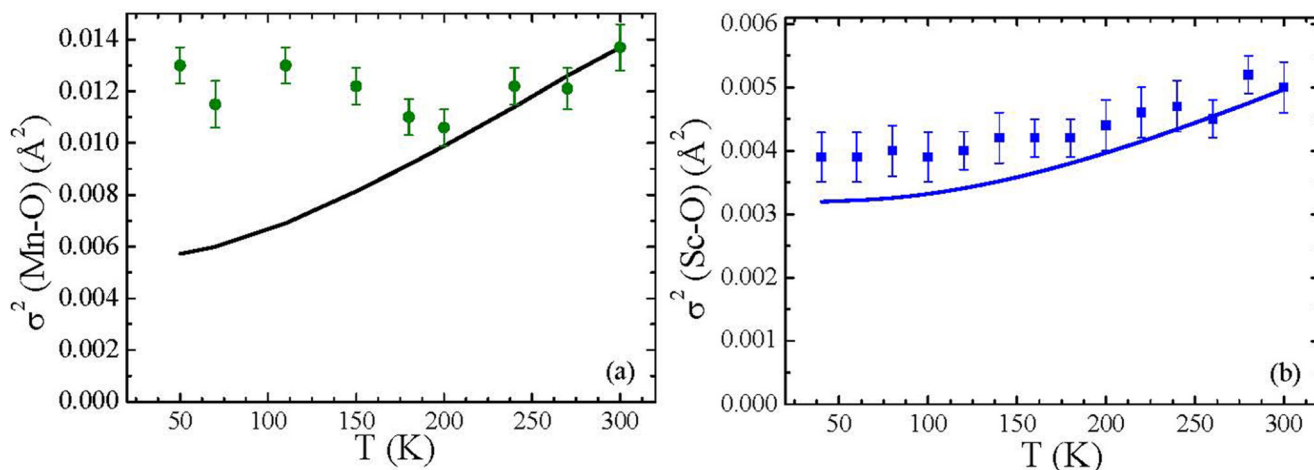|	Sc-O	$\sigma^2 \times 10^{-3}$(Å^2)	R_{factor}
LaScO$_3$	2.095(6)	2.9(9)	0.008
$x = 0.9$	2.101(6)	3.3(5)	0.009
$x = 0.6$	2.087(8)	3.5(6)	0.013
$x = 0.5$	2.089(6)	3.5(6)	0.008
$x = 0.4$	2.087(6)	3.2(5)	0.008
$x = 0.3$	2.10(1)	3.1(7)	0.01

FIG. 9. (Color online) Temperature evolution of σ^2 for $LaMn_{0.4}Sc_{0.6}O_3$ for (a) Mn-O and (b) Sc-O and the correlated Debye fit (line).

considering only one average Sc-O interatomic distance, in terms of the residual factor reported in Table III. The only difference is that lower Debye-Waller factors are obtained for the three different Sc-O distances. Thus, in order to fully disentangle thermal from any static disorder contribution, the temperature-dependent EXAFS spectra of $LaMn_{0.4}Sc_{0.6}O_3$ at the Mn and Sc K edge, between 80 and 300 K, were analyzed using the one-distance model in both cases.

Figures 9(a) and 9(b) show the Debye-Waller factors σ^2 for the Mn-O and Sc-O peak compared to the correlated Debye model fit, respectively. The amplitude reduction factor is fixed to 0.8 for Mn and to 0.9 for Sc K-edge fits, as a matter of comparison with the data shown previously. The values of σ^2 obtained for the Mn-O one-distance model are approximately five times bigger than the values obtained for a model of three pairs of Mn-O distances (see Table II). This validates the robustness of MnO_6 tetragonal distortion for $LaMn_{0.4}Sc_{0.6}O_3$ along this temperature range. In either case there is significant evidence of static distortion excess at low temperatures, as the evolution of σ^2 with temperature is rather constant within the experimental error bar. This result confirms the very little distortion of the ScO_6 octahedron, in agreement with the small orthorhombic distortion of $LaScO_3$ for all Sc concentrations.

IV. DISCUSSION AND CONCLUSIONS

The XRD results show that the tetragonal distortion of the MO_6 octahedron continuously decreases with the Sc content. There are two possibilities that could explain this fact: either both MnO_6 and ScO_6 octahedron are equally distorted, and the magnitude of the correlated distortion decreases with x, or the observed distortion of MO_6 by XRD corresponds to the average of different MnO_6 and ScO_6 octahedra. On the other hand, we recall here that the geometrical structure around the Mn(Sc) atom obtained from XAS at the Mn(Sc) K edge corresponds to the uncorrelated average of all the $MnO_6(ScO_6)$ octahedra. Therefore, the EXAFS results show that $LaMn_{1-x}Sc_xO_3$ is formed by tetragonal distorted MnO_6 and nearly regular ScO_6 octahedra. In order to correlate the two measurements, we have compared the M-O distances from XRD with the weighted addition of the Mn-O and Sc-O

distances taken from XRD for the end-member compounds of the series, $LaMnO_3$ and $LaScO_3$. The same comparison was also made with the weighted addition of the Mn-O and Sc-O distances determined by EXAFS for each Sc substitution. As shown in Fig. 10, the agreement is very good, which means that the tetragonal distortions of the MnO_6 octahedra are periodically ordered in the Sc-substituted compounds. Besides, assuming that the MnO_6 octahedra were randomly oriented, only one M-O interatomic distance would be obtained from XRD.

The occurrence of Mn tetragonal distortions, which remain ordered even up to high Sc content, has been also reported for the $TbMn_{1-x}Sc_xO_3$ diluted series [29]. However, the absence of larger distortion on ScO_6 octahedron is a surprising result, since Mn and Sc octahedra share vertices of the unit cell and the distortion would be expected to propagate from Mn to Sc and vice versa. One possibility is that the solid solution was not
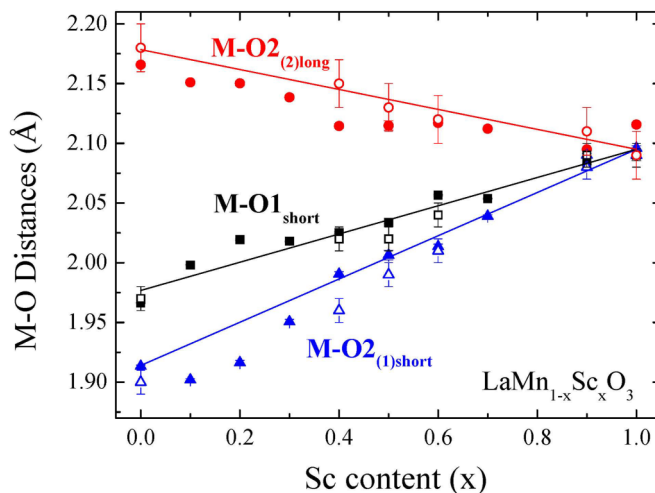

FIG. 10. (Color online) Evolution with the Sc content of the MO_6 octahedron from XRD (closed symbols) compared to the weighted addition of the Mn-O and Sc-O distances determined by EXAFS (open symbols). Lines indicate the weighted addition of the M-O distances from XRD of the two end-member compounds $LaMnO_3$ and $LaScO_3$.

random and some kind of phase segregation occurs in the Sc-substituted series. We have checked it but the XRD data do not show any trace of such a possibility, i.e., the diffraction peaks are well separated and the two phases cannot be identified. Therefore we will assume the formation of a random solid solution of Sc and Mn atoms, each of them maintaining its local structure. On the other hand, Ga substitution induces a drastic change in the crystallographic structure: the lattice parameters quickly converge to a unique parameter and the glide plane symmetry is nearly lost. In this case, the MnO_6 tetragonal distortion decreases with the Ga content in such a way that it disappears completely for $x \geqslant 0.6$.

In order to understand the different behavior of Sc series in comparison with the Ga-substituted series, it is worth comparing the crystallographic properties of the parent compounds: $LaMnO_3$, $LaGaO_3$, and $LaScO_3$. The three compounds adopt the orthorhombic distortion of the cubic perovskite structure. Following Landau theory, the orthorhombic structure can be considered as a distortion of the ideal cubic structure phase by condensation of certain phonons. It is well known that the transition from Pm-$3m$ to $Pbnm$ has a total of seven active modes belonging to the irreducible representations R_4^+, R_5^+, X_5^+, M_2^+, and M_3^+ [36]. Focusing on the oxygen sublattice, these modes operate as follows. The R_4^+ and M_3^+ modes are associated with the tilts of MO_6 octahedra along the [110] and [001] directions, respectively. The R_5^+ mode produces a distortion of the octahedron. The movement of equatorial oxygens is similar to the movement produced by the R_4^+ mode, but apical oxygens are displaced in antiphase, producing a trigonal distortion of the octahedral environment. The X_5^+ mode acts only on the apical oxygens that are shifted along the y direction. Finally, the M_2^+ mode acts only on the equatorial oxygens, and it is responsible for the Jahn-Teller distortion since it produces the approach of two oxygens to the central atom while the other two move away. From the structural data obtained in previous refinements [Table I, [6,37], we have performed the mode decomposition using the AMPLIMODES program [38] and determined the role of active modes in the transition from the ideal cubic perovskite (Pm-$3m$) to the distorted orthorhombic structure of the three compounds. The results are shown in Table IV.

The table shows that the main modes yielding to the distorted $LaMnO_3$ structure correspond to the rotations of the MnO_6 octahedron, which is a known mechanism to relieve strain in the perovskite structure when the atom at position A (La in this case) is too small in comparison to the atom in the B position (Mn). As secondary modes, we observe a

TABLE IV. Summary of distortion amplitudes (Å) of the active modes in the transition from an ideal cubic perovskite to the orthorhombic structures of the given compounds.

	$LaMnO_3$	$LaScO_3$	$LaGaO_3$
R_4^+	1.18	1.60	0.83
R_5^+	0.09	0.13	0.28
X_5^+	0.53	0.62	0.19
M_2^+	0.35	0.005	0.009
M_3^+	0.87	1.04	0.45

significant contribution X_5^+ and, as expected, the M_2^+ mode gives rise to the zigzag structure of Mn-O2 bond lengths in the ab plane of the $Pbnm$ cell. In $LaScO_3$, greater distortions are observed in all active modes except for the M_2^+ (Jahn-Teller) mode, which is strongly suppressed. This is because Sc^{3+} is bigger than Mn^{3+} and therefore, the concomitant structural strain is relaxed, with larger tilts of ScO_6 octahedra but also with slight distortion in the octahedral coordination. Instead, Sc has no $3d$ electrons and experiences no energy gain with the condensation of M_2^+ mode. On the other hand, the only significant modes in $LaGaO_3$ are the rotation modes (R_4^+ and M_3^+), in agreement with its nearly quasicubic structure and the occurrence of regular GaO_6 octahedra. The marked difference in the amplitude of the soft modes for $LaGaO_3$ and $LaScO_3$ explain their different behavior. On the one hand, MnO_6 is hardly distorted in an environment composed by regular GaO_6 octahedra, because the energy gain produced by MnO_6 distortion does not compensate the loss of elastic energy in the whole lattice. However, these distortion results are more feasible when MnO_6 is surrounded by ScO_6 octahedra, since the strong tilting of the ScO_6 octahedron allows the mixing of distorted MnO_6 and regular ScO_6 octahedra. The present results show that the occurrence of the tetragonal distortion of the MnO_6 octahedron strongly depends on the lattice in which the Mn atom is located. Moreover, the direction of the tetragonal distortion is also determined by the crystal structure of this lattice.

This structural study also has strong implications on the magnetism of these $LaMn_{1-x}B_xO_3$ [$B = (Ga/Sc)$] systems. As pointed out in the Introduction, the substitution of the Mn atom by a nonmagnetic atom such as Ga or Sc induces a ferromagnetic contribution, and for $x = 0.5$, a complete ferromagnetic state is achieved in both cases [22,23]. Despite the different structural behavior found for Ga and Sc substitutions, the magnetic response for $x \geqslant 0.5$ is similar in both cases, with the magnetization at 5 T being $\sim 3.4 \, \mu_B$/Mn. Two models have been reported to account for the change from the A-type antiferromagnetic ordering to the collinear ferromagnetic ordering: the spin flipping of Mn e_g orbital in JT-distorted Mn^{3+} atoms surrounded by Ga(Sc) atoms [24] and the FM vibronic superexchange interaction coming from disordered and fluctuating JT-distorted Mn^{3+} atoms [17]. The first model considers that e_g orbitals from Ga(Sc) nearest neighbors, contained originally in the ab plane, flip to be aligned along the c axis. According to Goodenough–Kanamori–Anderson rules, which determine the magnitude and sign of the magnetic exchange interactions based on the orbital arrangement [39], ferromagnetic interactions appear due to this orbital flip induced by Ga substitution. The second model proposes a monotonic transition from static to dynamic local Jahn-Teller distortions of the MnO_6 octahedra with increasing Ga/Sc concentration [17,19,25]. Superexchange vibronic interactions would then be responsible for the onset of ferromagnetism upon Ga or Sc doping.

Nevertheless, none of these two models can be supported by our structural study. As we showed in Refs. [26,27], the orthorhombic distortion in $LaMnO_3$ decreases continuously after Ga substitution and it disappears for $x > 0.5$, despite that the formal valence of the Mn atom is 3+. Besides, for $x < 0.5$, the local Jahn-Teller distortion remains ordered as in

$LaMnO_3$. We note here that the interaction time scale for an x-ray absorption process (fs) is shorter than for the thermal lattice vibrations, and no dynamic Jahn-Teller distortion was observed in the Ga-substituted samples, contrary to the dynamical distortion observed at T_{JT} in $LaMnO_3$ [28]. The case of Sc substitution is more striking. As it has been shown here, the orthorhombic distortion and its ordering remain unaltered with the Sc content, i.e., the effect of the Sc substitution is only a dilution of the Mn^{3+} lattice. Therefore, A-type antiferromagnetic ordering would be preserved if only nearest-neighbor magnetic interactions were considered. Since local structure effects are almost negligible in this last case, the change from an A-type antiferromagnet to a collinear ferromagnet in the Sc-substituted series must arise from the dilution effect with the Sc nonmagnetic ion.

The A-type ordering in $LaMnO_3$ is achieved by ferromagnetic interactions of Mn^{3+} moments within the *ab* plane and antiferromagnetic coupling between adjacent planes along the *c* direction. This structure was explained in terms of superexchange interactions and orbital ordering of Mn e_g orbitals in the *ab* plane forming zigzag chains. In this sense, it is not unexpected that dilution of Mn^{3+} with nonmagnetic Sc^{3+} preserves the ferromagnetic ordering within the *ab* plane; however, the disappearance of antiferromagnetism of adjacent planes resulting in a three-dimensional ferromagnet for $LaMn_{0.5}Sc_{0.5}O_3$ compound is surprising [23]. A qualitative explanation is given in Fig. 11. Two basis ingredients make up the superexchange interaction: the Pauli exclusion principle and Hund's rule. In a -Mn-O-Sc-O-Mn- chain, the usual Mn-O-Mn superexchange interaction is interrupted by a nonmagnetic ion without 3*d* electrons in which the Pauli term vanishes and only the Hund's energy may play a role in the hopping via the intermediate oxygen *p* orbital. The result is a weak but ferromagnetic second-neighbor exchange interaction between
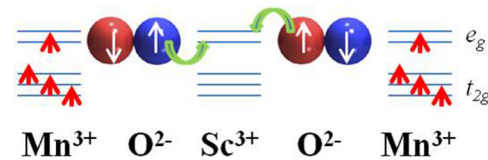

FIG. 11. (Color online) Mechanism of second-neighbor superexchange interaction mediated by oxygen *p* orbitals and a metal transition without *d* electrons.

the magnetic Mn atoms. On the other hand, the origin of ferromagnetism in the Ga series in which the Jahn-Teller distortion of the Mn^{3+} atoms disappears would be due to a change in the sign of the nearest-neighbor interactions.

Summarizing, the structural changes originated by the isovalent substitution of the Mn^{3+} atom in $LaMnO_3$ is completely different for Ga and Sc atoms. Ga substitution induces a continuous decreasing of the MnO_6 Jahn-Teller distortion, yielding regular octahedron for Ga content $\geqslant 0.5$. Sc substitution instead keeps the MnO_6 Jahn-Teller distortion and its ordering along the whole series. The appearance of ferromagnetism in the two series cannot be explained by the proposed models [17,24]. In particular, for the Sc-substituted samples, second-neighbor ferromagnetic interactions can account for this behavior.

[1] E. Dagotto, Science **318**, 1076 (2007).

[2] J. B. Goodenough, *Magnetism and Chemical Bond* (Interscience, New York, 1963).

[3] E. O. Wollan and W. C. Koehler, Phys. Rev. **100**, 545 (1955).

[4] Q. Huang, A. Santoro, J. W. Lynn, R. W. Erwin, J. A. Borchers, J. L. Peng, and R. L. Greene, Phys. Rev. B **55**, 14987 (1997).

[5] J. B. A. A. Elemans, B. Van Laar, K. R. Vand Der Veen, and B. O. Loopstra, J. Solid State Chem. **3**, 238 (1971).

[6] C. Ritter, M. R. Ibarra, J. M. De Teresa, P. A. Algarabel, C. Marquina, J. Blasco, J. García, S. Oseroff, and S. W. Cheong, Phys. Rev. B **56**, 8902 (1997).

[7] E. Dagotto, J. Hotta, and A. Moreo, Phys. Rep. **344**, 1 (2001).

[8] M. B. Salamon and M. Jaime, Rev. Mod. Phys. **73**, 583 (2001).

[9] C. Meneghini, C. Castellano, S. Mobilio, A. Kumar, S. Ray and D. D. Sarma, J. Phys.: Condens. Matter **14**, 1967 (2002).

[10] A. Lanzara, N. L. Saini, M. Brunelli, F. Natali, A. Bianconi, P. G. Radaelli, S.-W. Cheong, Phys. Rev. Lett. **81**, 878 (1998).

[11] C. Zener, Phys. Rev. **82**, 403 (1951).

[12] H. A. Jahn and E. Teller, Proc. R. Soc. London, Ser. A **161**, 220 (1937).

[13] A. Abragam and B. Bleaney, *Electron Paramagnetic Resonance of Transition Ions* (Clarendon, Oxford, 1970), p. 792.

[14] A. J. Millis, R. Mueller, and B. I. Shraiman, Phys. Rev. B **54**, 5405 (1996).

[15] J. B. Goodenough, A. Wold, R. J. Arnott, and N. Menyuk, Phys. Rev. **124**, 373 (1961).

[16] J. Töpfer and J. B. Goodenough, Eur. J. Sol. State Inorg. Chem. **34**, 467 (1997).

[17] J.-S. Zhou, H. Q. Yin, and J. B. Goodenough, Phys. Rev. B **63**, 184423 (2001).

[18] S. Hébert, C. Martin, A. Maignan, R. Retoux, M. Hervieu, N. Nguyen, and B. Raveau, Phys. Rev. B **65**, 104420 (2002).

[19] J. B. Goodenough, R. I. Dass, and J. Zhou, Solid State Sci. **4**, 297 (2002).

[20] M. C. Sánchez, J. García, J. Blasco, G. Subías, and J. Pérez-Cacho, Phys. Rev. B **65**, 144409 (2002).

[21] J. Blasco, J. García, M. C. Sánchez, G. Subías, J. Campo, and J. Pérez-Cacho, Eur. Phys. J. B **30**, 469 (2002).

[22] J. Blasco, J. García, J. Campo, M. C. Sánchez, and G. Subías, Phys. Rev. B **66**, 174431 (2002).

[23] J. Blasco, V. Cuartero, J. García, and J.A. Rodríguez-Velamazán, J. Phys.: Condens. Matter **24**, 076006 (2012).

[24] J. Farrell and G. A. Ghering, New J. Phys. **6**, 168 (2004).

[25] J-S. Zhou and J. B. Goodenough, Phys. Rev. B **68**, 144406 (2003).

[26] M. C. Sánchez, G. Subías, J. García, and J. Blasco, Phys. Rev. B **69**, 184415 (2004).

[27] M. C. Sánchez, G. Subías, J. García, and J. Blasco, Phys. Rev. B **73**, 094416 (2006).

[28] M. C. Sánchez, G. Subías, J. García, and J. Blasco, Phys. Rev. Lett. **90**, 045503 (2003).

[29] V. Cuartero, J. Blasco, J. García, G. Subías, C. Ritter, and J. A. Rodríguez-Velamazán, Phys. Rev. B **81**, 224117 (2010).

[30] J. Rodríguez-Carvajal, Physica B **192**, 55 (1993); J. Rodríguez-Carvajal and T. Roisnel, https://www.ill.eu/sites/fullprof/.

[31] A. Di Cicco, G. Aquilanti, M. Minicucci, E. Principi, N. Novello, A. Cognigni, and L. Olivi, J. Phys.: Conf. Series **190**, 012043 (2009).

[32] B. Ravel and M. Newville, J. Synchrotron Radiat. **12**, 537 (2005).

[33] J. J. Rehr and R. C. Albers, Rev. Mod. Phys. **72**, 621 (2000).

[34] J. García, G. Subías, V. Cuartero, and J. Herrero-Martín, J. Synchrotron Radiat. **17**, 386 (2010).

[35] Y. Joly, D. Cabaret, H. Renevier, and C. Natoli, Phys. Rev. Lett. **82**, 2398 (1999).

[36] C. J. Howard and H. T. Stokes, Acta Cryst. B **54**, 782 (1998).

[37] M. Kajitani, M. Matsuda, A. Hoshikawa, K. Oikawa, S. Torii, T. Kamiyama, F. Izumi, and M. Miyake, Chem. Mater. **15**, 3468 (2003).

[38] J. M. Perez-Mato, D. Orobengoa, and M.I. Aroyo, Acta Cryst. A **66**, 558 (2010).

[39] J. B. Goodenough, J. Phys. Chem. Solids **6**, 287 (1958); J. Kanamori, *ibid.* **10**, 87 (1959).